

VIP Very Important Paper

Special Collection

www.batteries-supercaps.org

Hierarchical Carbon Nanosheet Embedded MnO_x Cathode for High-Performance Aqueous Zinc-Ion Batteries

Shimeng Zhang⁺^[a], Xiaoqi Wang⁺^[b, c], Jianbo Li,^[a] Yuwei Chen,^[a] Yu Wu,^[a] Shengchi Bai,^[c] Xu Jin,^[c] Bowen Jin,*^[a] and Mingfei Shao*^[a]

Aqueous zinc-ion battery is one of the candidates for the next generation batteries due to its reliable safety, environmental friendliness and low cost. While the poor structurally stability and limited cyclic reversibility of the cathode restricts its practical application. In this work, we elaborately design hierarchical three-dimensional (3D) carbon networks (CNS) for the embedding of non-stoichiometry MnO_x with abundant defects (MnO_x/CNS), which provide 3D diffusion pathway and

efficient electrochemical active sites for zinc-ion storage. The as-designed Zn//MnO_x/CNS battery delivers high energy density of 452.2 Wh kg⁻¹ at a power density of 133.0 W kg⁻¹, much superior to that of MnO₂/CNS and pristine MnO₂. Moreover, defective manganese species experience stable phase transformation during charging/discharging process, providing a long-term cycling performance with a high reversible capacity of 263.3 mAh g⁻¹ at 1 A g⁻¹ after 1000 cycles.

Introduction

Lithium-ion batteries (LIBs) presently dominate the markets of rechargeable battery for portable devices due to their inherent advantages including high specific capacity and voltage, excellent cycling performance, and high energy density.^[1–4] Unfortunately, limited resources and increasing price of lithium restrict their large-scale practical applications in the near future.^[5] Moreover, the organic electrolytes used in LIBs are generally toxic and flammable, which likely cause huge safety issues.^[6–9] Therefore, development of non-lithium battery technology with high safety and cost effectiveness is highly desirable.^[10,11] In this regard, zinc-ion batteries (ZIBs) that use nonflammable aqueous electrolytes represent a promising candidate capable of enabling intrinsic safety.^[12,13] Moreover, the abundant natural resources and cost effectiveness of Zn exhibit great potential in large-scale energy storage.^[14–16] However, the strong electrostatic interaction between bivalent Zn²⁺ and host materials in repeating intercalation/deintercalation process in ZIBs, leads to low capacity, serious structural distortion, and capacity decay.^[17] Therefore, development of

high-performance electrode materials for ZIBs is urgently required.

To date, various cathode materials have been explored to couple with Zn anode, among which MnO₂ has attracted significant research attention due to its cost effectiveness, environmental friendliness, and high theoretical capacity.^[18–24] MnO₂ shows various crystal structures, i.e., α -MnO₂, β -MnO₂, γ -MnO₂, δ -MnO₂, and spinel-type MnO₂. However, a theoretical capacity of 308 mAh g⁻¹ has barely been achieved for MnO₂.^[25] One of the main reasons is the intrinsic low ionic conductivity of MnO₂ due to its narrow ionic channels. The electrostatic repulsion of ions from host hinders Zn²⁺ transportation and intercalation, resulting in the disappointing rate capability.^[26] Besides, the formation of irreversible phase of MnO₂ during long-term cycling also limits its practical application.^[14,27,28] Previous related studies indicated that doping heteroatom into the host materials is an effective approach to enhance its electrical conductivity and suppress dissolution of the manganese(II) ions.^[29–35] However, the existing Zn-MnO₂ batteries are still far from meeting the demand of practical applications. In this regard, it is speculated that the atomic-level structure engineering can lead to changes in chemical and physical properties, which can improve the energy storage performance and cycling life as well.^[36–48] However, designing MnO₂ cathodes at atomic-level scale with higher power and energy density still holds a huge challenge.

Herein, defective MnO_x cathodes were elaborately designed based on hierarchical three-dimensional (3D) carbon networks (MnO_x/CNS). The integrated carbon frameworks provide 3D diffusion path and electrochemical active sites, exhibiting superior electronic and ionic conductivity. Moreover, the defective MnO_x with rich cation vacancies leads to effective enhancement in the reversibility and kinetics of Zn²⁺ intercalation/deintercalation. Moreover, defective Mn species exhibit stable phase transformation during charging/discharging process and thus achieves long cycling life. The assembled aqueous

[a] S. Zhang,⁺ J. Li, Y. Chen, Y. Wu, B. Jin, M. Shao
State Key Laboratory of Chemical Resource Engineering, Beijing University of Chemical Technology, Beijing 100029, P. R. China.
E-mail: bwjin@buct.edu.cn
shaomf@mail.buct.edu.cn

[b] X. Wang⁺
School of Chemistry and Chemical Engineering, Beijing Institute of Technology, Beijing 100081, P. R. China.

[c] X. Wang,⁺ S. Bai, X. Jin
Research Center of New Energy, PetroChina Research Institute of Petroleum Exploration & Development, Beijing 100083, P. R. China.

[+] These authors contributed equally to this work.

Supporting information for this article is available on the WWW under
<https://doi.org/10.1002/batt.202200476>

An invited contribution to a Special Collection on IV Symposium on Advanced Energy Storage

ZIB delivers excellent specific capacity of 340 mAh g^{-1} at 0.1 A g^{-1} for 50 cycles and 184.3 mAh g^{-1} at 1 A g^{-1} for 1000 cycles, exhibiting remarkable performance in terms of power and energy density and superior cycling stability.

Results and Discussion

The fabrication process of MnO_x/CNs is illustrated in Figure 1(a). Before the growth of manganese oxides, “integrated 3D CNs”, i.e., carbon nanosheets arrays were fabricated, which could be used as current collector to anchor MnO_x . The CNs were prepared by the *in situ* growth of zeolitic imidazolate framework (ZIF-67) on the surface of CoAl-LDH arrays (denoted as

CoAl-LDH@ZIF-67) followed by a subsequent carbonization and acid treatment.

First, the CoAl-LDH arrays were *in situ* grown on the hydrophilic carbon cloth *via* hydrothermal treatment. Figure 1(b) shows that the hexagonal thin nanosheet arrays are uniformly distributed on the carbon cloth (CC) after hydrothermal treatment. Further, the CoAl-LDH@ZIF-67 composite material was synthesized by *in situ* polymerization through a facile electrochemical deposition in a solution containing cobalt nitrate and 2-methylimidazole (MeIM). Benefiting from the abundance of metal sites and oxygen-containing functional groups of LDH, ZIF-67 crystals with a diameter of $\sim 30 \text{ nm}$ were tightly attached and fixed on both sides of CoAl-LDH arrays (Figure 1c). Then, as-obtained CoAl-LDH@ZIF-67 was further

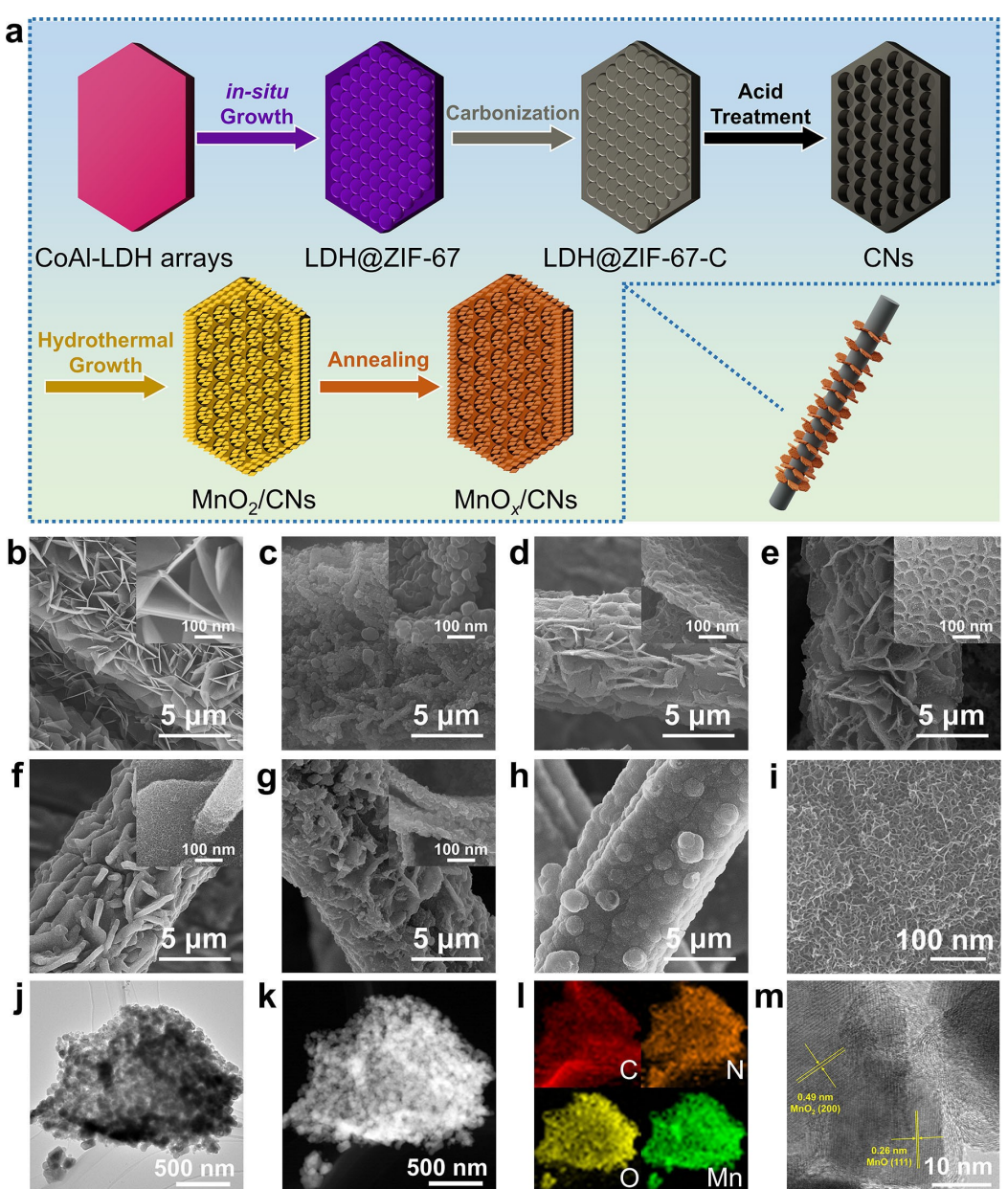


Figure 1. a) Schematic diagrams of the synthesis of MnO_x/CNs . SEM images of b) CoAl-LDH arrays, c) LDH@ZIF-67, d) LDH@ZIF-67-C, e) CNs, f) MnO_2/CNs , g) MnO_x/CNs , and h, i) MnO_2/CC . j) TEM image, k, l) TEM EDX mapping image, and m) HRTEM image of MnO_x/CNs .

subjected to carbonization in a controlled-atmosphere furnace under nitrogen gas flow at 800 °C for 2 h (the resulting product is denoted as LDH@ZIF-67-C), in which the ZIF-67 shell transformed to porous graphitic carbon (Figure 1d). Finally, the above-mentioned carbon material was acid-treated with dilute hydrochloric acid at room temperature, and then the Co particles and other spinels were etched to achieve the integrated 3D CNs. The XRD patterns of as-prepared samples confirmed the successful synthesis process (Figure S1).

Figure 1(e) shows the porous carbon nanosheet arrays with size of ~3 μm, vertically aligned on the carbon fiber. These carbon nanosheets with dense porosity (pore diameters of 50–100 nm) exhibited large surface area for loading MnO_x and provided fast ions/electron transfer ability. After a facile *in situ* hydrothermal growth, secondary hierarchical MnO_x nanosheets with length of ~50 nm and thickness of ~5 nm grew uniformly on CNs surface (Figure 1f). Finally, MnO_x/CNs was formatted under a low-temperature (500 °C) treatment in N₂ for improving the combination between MnO₂ and CNs. Figure 1(g) illustrates that the similar framework of hierarchical nanosheet of MnO_x/CNs is still maintained after annealing. As a reference for comparative analysis, the MnO₂ array on bare carbon cloth was fabricated by the same hydrothermal approach followed by annealing (Figure 1h and i). The results indicate that MnO₂ densely covers the carbon fiber, instead of forming arrays or multistage structures. The transmission electron microscopy (TEM) results also confirm the successful anchoring of nano-

particles with size of ~50 nm on CNs substrate (Figure 1j). Furthermore, the TEM combined with energy dispersive X-Ray mapping clearly verifies the homogeneous distribution of various elements (C, N, Mn, and O), indirectly indicating the successful fabrication of MnO_x/CNs hierarchical structure (Figure 1k and l). The high-resolution TEM (HRTEM) characterization was carried to further study the crystallographic difference between MnO₂/CNs and defective MnO_x/CNs. The results indicate that the spacing of lattice fringe of MnO₂/CNs in HRTEM image is about 0.31 nm, belonging to the (310) plane of α-MnO₂ (Figure S2).^[24] More interestingly, the different lattice fringes spacings of 0.49 and 0.26 nm are observed in MnO_x/CNs, which is consistent with the (200) planes of α-MnO₂ and (111) planes of MnO, respectively, indicating the successful formation of MnO_x (Figure 1m).

Furthermore, the above-mentioned conclusion is also supported by the XRD patterns (Figure 2a). For MnO₂/CC and MnO_x/CNs, three diffraction patterns located at $2\theta = 12.7^\circ$, 37.5° , and 42.5° are observed, which, respectively, match well with the (110), (211), and (301) planes of tetragonal α-MnO₂ [PDF#44-0141]. For MnO_x/CNs, additional diffraction signals emerge at 34.9° , 40.5° , and 58.7° , which are, respectively, indexed to the (111), (200), and (220) planes of MnO [PDF#07-0230], *i.e.*, hybrid phase of MnO_x existed in MnO_x/CNs. Raman spectra display the presence of D band (1352 cm^{-1}) and G band (1600 cm^{-1}) in CNs, where I_D/I_G ratio equals 1.12 (Figures 2b and S3). The high ratio in CNs characterizes its defective nature,

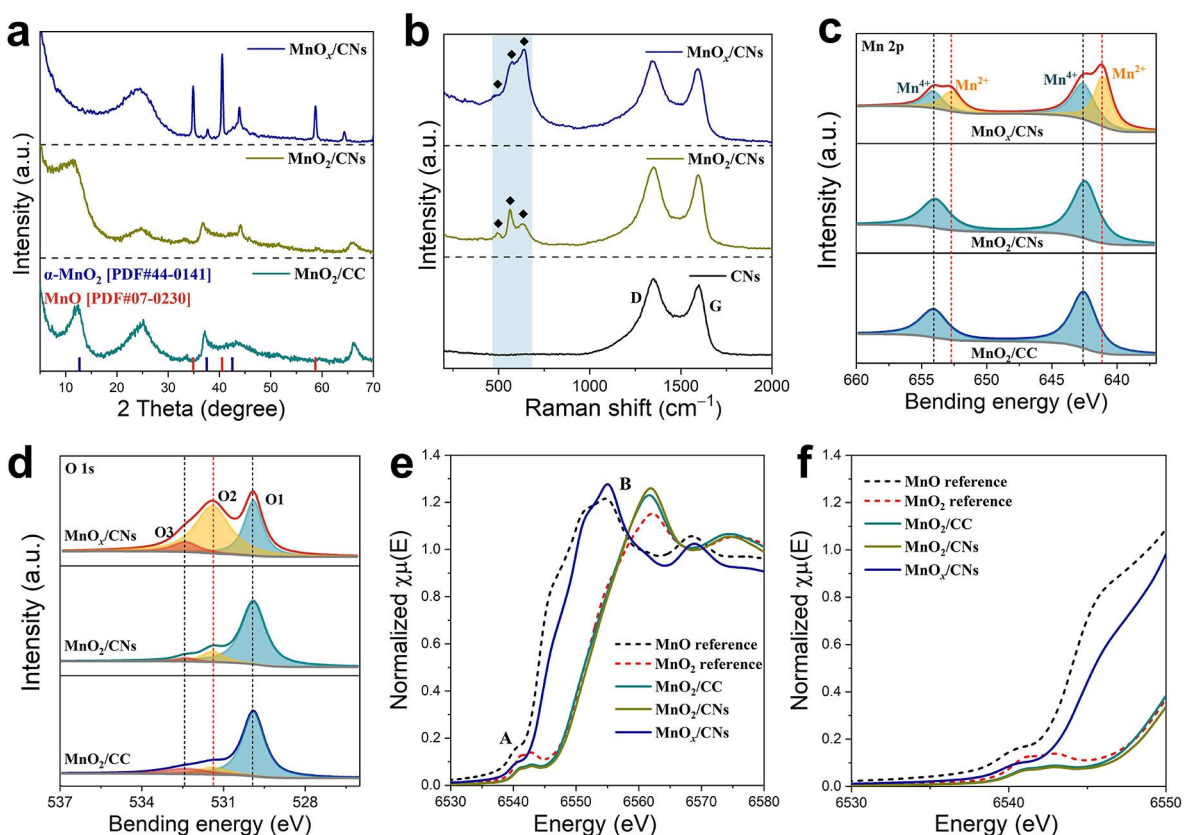


Figure 2. a) XRD patterns, b) Raman spectra, c, d) high-resolution Mn and O XPS spectra, and e, f) Mn K-edge XANES spectra of as-prepared samples.

which is conducive to anchoring MnO_2 . As expected, the $I_{\text{D}}/I_{\text{G}}$ ratio decreases to 1.06 after deposition of MnO_2 , which clearly indicates that MnO_2 was mainly deposited on the defects of CNs. Moreover, three peaks at 644, 570, and 495 cm^{-1} are observed in Raman spectrum, which are attributed to the stretching vibration of MnO_6 groups in $\alpha\text{-MnO}_2$ and stretching vibration of Mn–O bond, respectively. After annealing treatment, these peaks are widened and get shifted to high wave numbers for the MnO_x/CNs sample due to oxygen vacancy.

The high-resolution Mn 2p X-ray photoelectron spectroscopy (XPS) results of MnO_2/CC and MnO_2/CNs exhibit that the spectra split into doublet strong peaks at 654.0 and 644.6 eV, which can be attributed to Mn^{4+} (Figures 2c and S4).^[41] Compared to MnO_2/CC and MnO_2/CNs , new doublet peaks are observed at 652.7 and 641.1 eV for MnO_x/CNs , which correspond to the characteristics peaks of Mn^{2+} , thus proving that part of Mn(IV) was reduced to Mn(II) after annealing. The high-resolution O 1s spectra exhibit three typical peaks at 529.9, 531.4, and 532.5 eV, representing lattice oxygen (O1), oxygen vacancy (O2), and oxygen species adsorbed on surface (O3), respectively (Figure 2d).^[49] For MnO_2/CC and MnO_2/CNs , strong characteristic peak of lattice oxygen and weak peaks of oxygen vacancy and oxygen species adsorbed on surface are observed. Differently, the characteristics peak of oxygen vacancy is significantly enhanced in MnO_x/CNs , thus confirming the increase of oxygen vacancy after annealing. The extended X-ray absorption fine structure (EXAFS) of Mn K-edge was measured to analyze the MnO_2 on integrated MnO_x/CNs in order to determine the change in the local and electronic structure. A series of normalized Mn K-edge XANES spectra is shown in Figure 2(e and f). A weak pre-edge peak (A) is attributed to transition of a 1 s electron to an unoccupied 3d orbital. Owing to the dipole selection rule, this transition is forbidden in an octahedral symmetry. Nonetheless, the transition is partially allowed owing to the mixing of 3d–4p orbitals, which originates from the slightly distorted MnO_6 octahedral units. Simultaneously, the main peak B is ascribed to the dipole-allowed transition from 1 s electron to 4p orbital. Moreover, the reduction of MnO_x/CNs produces a shift in the position of absorption edge toward a lower energy, indicating higher average electron density than that of MnO_2/CNs , where MnO_2 standard is used as the reference.

The electrochemical performance of electrode was studied using ZIBs with 2 M $\text{ZnSO}_4 + 0.2$ M MnSO_4 aqueous solution. Figure 3(a) presents the cyclic voltammetry (CV) curves at the second cycle and a scan rate of 0.1 mVs^{-1} in the voltage window of 1.0–1.8 V. Clearly, all CV curves expose two pairs of strong redox peaks, which can be attributed to the reversible intercalation/deintercalation of H^+ or Zn^{2+} into/from the interlayer host, respectively. Correspondingly, the valence of Mn switches between Mn^{4+} and Mn^{3+} during charging/discharging process. Noteworthy, the separation between reducing peak to oxidation peak of MnO_x/CNs is 184 and 323 mV, which is smaller than that of MnO_2/CNs and MnO_2/CC , demonstrating highly reversible and better electrochemical reactivity of MnO_x/CNs . Figure 3(b) depicts the galvanostatic charge and discharge (GCD) curves of MnO_x/CNs , MnO_2/CNs ,

and MnO_2/CC electrodes at the current density of 0.1 Ag^{-1} , where two discharge plateaus are observed at about 1.32 and 1.2 V, respectively. The MnO_x/CNs electrode delivers the highest discharge capacity of 342 mAh g^{-1} and the smallest potential gap between charge and discharge plateaus. This result further confirms its limited electrochemical overpotential and improved reaction kinetics. Moreover, this result is in good agreement with the CV analysis.

The electron transfer process during the charging/discharging process was studied through electrochemical impedance spectroscopy (EIS). Figure 3(c) displays the Nyquist impedance plots of MnO_x/CNs , MnO_2/CNs , and MnO_2/CC electrode, which consist of semicircle in the high-frequency region and slant line in the low-frequency region. The charge transfer resistance (R_{ct}) of the MnO_x/CNs electrode is 37.7 Ω , which is more than 2 times lower than that of MnO_2/CNs electrode (91.0 Ω) and MnO_2/CC electrode (105.4 Ω), clarifying the occurrence of faster ion/electron transportation. Moreover, the fast electron transfer process of MnO_x/CNs also enhances the electrochemical performance at high charging rate. Figure 3(d) shows the charge-discharge profiles of the MnO_x/CNs electrode under different current densities from 0.1 to 2 Ag^{-1} in the potential range of 0.8 to 1.8 V. Noteworthy, the potential gap between the charge and discharge plateaus widens with increasing current rate. However, the discharge plateaus can still be obtained even at a high current density of 2 Ag^{-1} , further confirming the excellent reaction kinetics in MnO_x/CNs electrode. The capacity of electrolyte calculated by using the GCD plots are presented in Figure 3(e). Highly reversible specific capacities of 342, 308.7, 276.8, 258.7, 226.1, and 175.3 mAh g^{-1} are delivered by MnO_x/CNs electrode at 0.1, 0.2, 0.5, 1.0, and 2.0 Ag^{-1} , respectively, which are significantly higher than those of MnO_2/CNs and MnO_2/CC samples. In order to investigate the capacity contribution of CNs in composite electrodes, pure CNs were assembled into Zn//CNs cells and tested (Figure S5a and b). Consequently, only $\sim 0.015 \text{ mAh cm}^{-2}$ of reversible capacity was provided at 1 mA cm^{-2} .

Moreover, the cyclic performance of MnO_x/CNs , MnO_2/CNs , and MnO_2/CC samples was evaluated at 0.1 Ag^{-1} in long cyclic process (Figure 3f). Notably, assembled battery based on MnO_x/CNs cathode delivers a high initial specific capacity of 342.8 mAh g^{-1} at low charging rate of 0.1 Ag^{-1} ; therefore, 340 mAh g^{-1} still remains after 50 cycles. In contrast, relatively low initial specific capacity of 288.5 and 262.3 mAh g^{-1} is obtained for MnO_2/CNs and MnO_2/CC , respectively, which fades rapidly in the following 50 cycles. Specific capacities of only 159.0 and 115.9 mAh g^{-1} are left, that is 55.1% and 44.2% of initial capacity, respectively. For cyclic process under high charging rate, MnO_x/CN also exhibits higher reversible capacity and more stable cycle ability compared with the MnO_2/CNs , and MnO_2/CC electrodes (Figure 3g). Moreover, MnO_x/CNs possess reversible capacity of 263.3 mAh g^{-1} (capacity retention of 91.2%) and high Coulombic efficiency of 99.7% even after 1000 cycles at 1 Ag^{-1} , which are much superior to those of MnO_2/CNs . Furthermore, MnO_2/CC assembled batteries that provided low capacity retention of 41.2% (184.3 mAh g^{-1}) and 30.2% (84.8 mAh g^{-1}), respectively. Accordingly, comprehensive

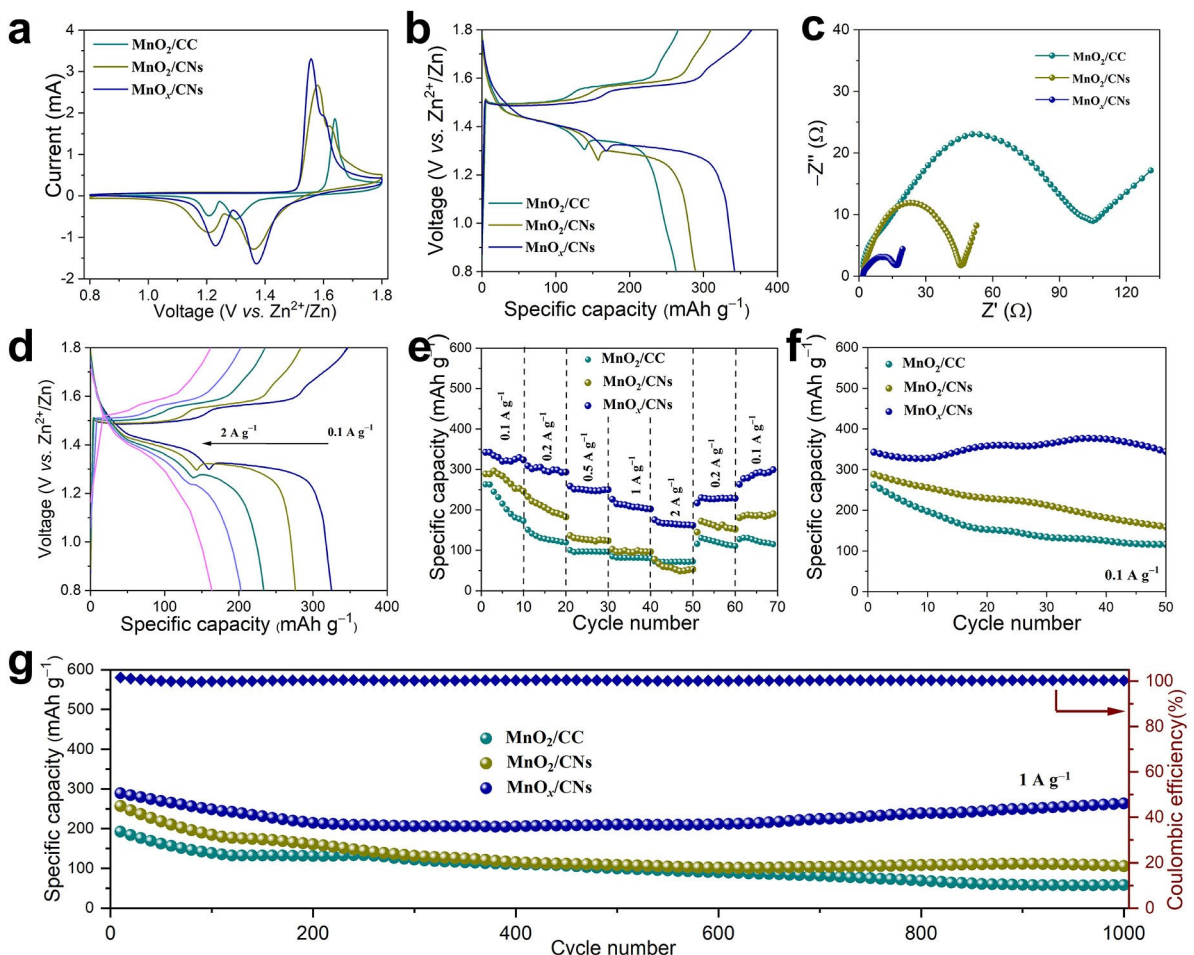


Figure 3. a) CV curves, b) GCD curves, and c) Nyquist impedance plots of full cells for different electrodes. d) GCD curves of MnO_x/CNs electrode from 0.1 to 2 A g^{-1} . e) Rate cycling of different electrodes from 0.1 to 2 A g^{-1} . f, g) Specific capacities of different electrodes at 0.1 A g^{-1} and 1 A g^{-1} .

analysis of SEM images shows no structural collapse or changes of the hierarchical 3D features after cycling, indicating the high structure stability of MnO_x/CNs electrode (Figure S6). To verify the superiority of the unique hierarchical 3D structure, Zn/MnO_x (powder) and $\text{Zn}/\text{MnO}_x/\text{CC}$ cells were also studied, as shown in Figures S7 and S8. Noteworthy, the discharge capacities of Zn/MnO_x (powder) and $\text{Zn}/\text{MnO}_x/\text{CC}$ at 1 A g^{-1} are only 60 and 137 mAh g^{-1} , respectively, much lower than that of $\text{Zn}/\text{MnO}_x/\text{CNs}$.

For the comprehensive understanding of the storage mechanism of Zn^{2+} in MnO_x/CNs electrode, crystal phase and structure changes during intercalation/deintercalation process were systematically monitored by *ex situ* XRD. Figure 4(a) shows the charge and discharge curve of the battery in 2 M ZnSO_4 and 0.2 M MnSO_4 electrolyte with current density of 300 mA g^{-1} . The battery was first discharged to 0.8 V (states i and ii), then charged to 1.8 V (states I to IV), and then finally discharged to 0.8 V (states IV to VII), and the corresponding *ex situ* XRD results are shown in Figure 4(b). In the diffraction pattern (belonging to MnO), peaks at 35° and 41.0° disappear, and the signal of $\alpha\text{-MnO}_2$ phase is enhanced after initial discharge cycle, which indicate disproportionate transformation of unique defective MnO_x to $\alpha\text{-MnO}_2$ phase. During discharg-

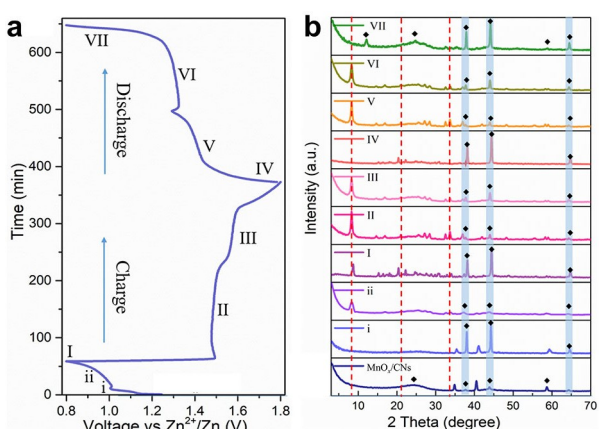


Figure 4. a) GCD curves of MnO_x/CNs electrode at 300 mA g^{-1} . b) *ex-situ* XRD patterns of MnO_x/CNs electrode during charge/discharge.

ing, the diffraction pattern of $\alpha\text{-MnO}_2$ phase shifts to a low angle, indicating that the interlayer spacing widened due to the intercalation of cations. In the charging process, the intercalated cations were drawn out from cathodes, and the $\alpha\text{-MnO}_2$ phase shifts back to the high angle. The periodic shift

and recovery of the layer spacing indicates that the intercalation and deintercalation of Zn^{2+} are reversible and do not bring about the destruction of the layered structure. Furthermore, the signals at 8.32° , 21.1° , and 33.8° can be observed in the following discharging process, which is attributed to the formation of $Zn_4SO_4(OH)_6 \cdot nH_2O$ [PDF# 44-0673]. This phenomenon should be related to the accompanied H^+ intercalation of $\alpha\text{-MnO}_2$, which provides enriched OH^- that combines with Zn^{2+} and SO_4^{2-} . Noteworthy, the peaks corresponding to $Zn_4SO_4(OH)_6 \cdot nH_2O$ disappeared after being fully charged, which indicates that the generation of by-product did not affect the stability of MnO_x/CNs . The result indicates that this newly formed $\alpha\text{-MnO}_2$ phase provides a fine layer structure and better structural stability, which can accommodate reversible Zn^{2+} intercalation and deintercalation.

A series of electrochemical tests was carried out to further recognize the excellent electrochemical performance of the MnO_x/CNs cathode. The CV curves at different scan rates are presented in Figure S9(a and b). Based on the Dunn's method, that is, $i = av + bv^{0.5}$, the current density in CV plots can be divided into pseudocapacitive-controlled and diffusion-limit. To be specific, when the scan rate is increased from 0.1 to 1.0 mVs^{-1} , the capacitive contribution of MnO_x/CNs increases significantly from 58.6% to 89.8%, much higher than that of MnO_2/CC (from 46.9% to 69.9%) (Figure S9c and d). Moreover, by using the Randles-Sevcik Equation, that is, $j_p = 268600n^{3/2}ACD^{1/2}v^{1/2}$, the diffusion rate can be calculated by using the slope of $j_p - v^{1/2}$ images (Figure S10a-d), where j_p is peak current density in amps, n is number of electrons transferred in redox event, A is electrode area in cm^2 , C is concentration in $mol\text{ cm}^{-3}$, D is diffusion rate in $cm^2\text{ s}^{-1}$, v is scan rate in $V\text{ s}^{-1}$, and reaction temperature is 25°C . The calculated diffusion rate of cations in MnO_x/CNs is in the range of $0.48\text{--}3.69 \times 10^{-8}\text{ cm}^2\text{ s}^{-1}$ during intercalation/deintercalation process, which is more than 4 times higher than that of MnO_2/CC ($0.13\text{--}0.77 \times 10^{-8}\text{ cm}^2\text{ s}^{-1}$) (Figure S10e). The Nyquist impedance plots of cells at different temperatures are exhibited in Figure S11(a and b). The R_{ct} of MnO_x/CNs is in the range of $10\text{--}20\ \Omega$ at $25\text{--}45^\circ\text{C}$, which is just one fifth of that of MnO_2/CC . Figure S11(c) shows the corresponding activation energy (E_a) that is calculated to be 14.2 kJ mol^{-1} for MnO_x/CNs by linear fitting by using Arrhenius equation, where $\ln(1/R_{ct}) = \ln A - E_a/RT$, which is lower than that of MnO_2/CC (22.1 kJ mol^{-1}), indicating the faster reaction kinetics and excellent electrochemical performance. For the further systematic exploration of the potential application of MnO_x/CNs in practical wearable devices, flexible quasi-solid ZIB with large area based on MnO_x/CNs cathode was fabricated. Two devices connected in series could continuously power a red LED (Figure S12). Moreover, the as-assembled ZIB also displays a favorable mechanical property, which can be used in both straight and bent states, indicating the potential applications in flexible devices.

Conclusion

In this study, a defective MnO_x cathode based on three-dimensional carbon networks (MnO_x/CNs) is reported. Elaborate integrated 3D CNs were used to establish an excellent conductive framework, which promoted the rapid conduction of electrons and ions. As-deposited MnO_x was anchored on CNs with plentiful defect, which enhanced the activities and kinetics of the intercalation/deintercalation of Zn^{2+} . The *ex situ* XRD technology confirms that MnO_x/CNs also maintained better structural stability and phase transition reversibility. The $Zn//MnO_x/CNs$ battery delivers a high energy density of 452.2 Wh kg^{-1} at power density of 133.0 W kg^{-1} , and long-term cycling performance with a high reversible capacity of 263.3 mAh g^{-1} at 1 Ag^{-1} after 1000 cycles, which make it a potential candidate to be used in commercial practical application.

Acknowledgements

This work was supported from the National Natural Science Foundation of China (21922501), China Postdoctoral Science Foundation (2021 M700350) and Research Funds for the Central Universities (ZY2118).

Conflict of Interest

The authors declare no conflict of interest.

Data Availability Statement

The data that support the findings of this study are available from the corresponding author upon reasonable request.

Keywords: carbon networks · defect engineering · high energy density cathodes · manganese-based cathodes · zinc-ion batteries

- [1] Q. Ni, B. Kim, C. Wu, K. Kang, *Adv. Mater.* **2022**, *34*, 2108206.
- [2] Y. Yuan, J. Yang, Z. Liu, R. Tan, M. Chuai, J. Sun, Y. Xu, X. Zheng, M. Wang, T. Ahmad, N. Chen, Z. Zhu, K. Li, W. Chen, *Adv. Energy Mater.* **2022**, *12*, 2103705.
- [3] Y. Chen, Y. Kang, Y. Zhao, L. Wang, J. Liu, Y. Li, Z. Liang, X. He, X. Li, N. Tavajohi, B. Li, *J. Energy Chem.* **2021**, *59*, 83–99.
- [4] J. Lei, Y. Yao, Z. Wang, Y.-C. Lu, *Energy Environ. Sci.* **2021**, *14*, 4418.
- [5] M. E. Pam, D. Yan, J. Yu, D. Fang, L. Guo, X. L. Li, T. C. Li, X. Lu, L. K. Ang, R. Amal, Z. Han, H. Y. Yang, *Adv. Sci.* **2021**, *8*, 2002722.
- [6] P. Ruan, S. Liang, B. Lu, H. J. Fan, J. Zhou, *Angew. Chem. Int. Ed.* **2022**, *61*, e202200598.
- [7] L. Godeffroy, I. Aguilar, J. Médard, D. Larcher, J.-M. Tarascon, F. Kanoufi, *Adv. Energy Mater.* **2022**, *12*, 2200722.
- [8] S. Islam, M. H. Alfaruqi, D. Y. Putro, S. Park, S. Kim, S. Lee, M. S. Ahmed, V. Mathew, Y.-K. Sun, J.-Y. Hwang, J. Kim, *Adv. Sci.* **2021**, *8*, 2002636.
- [9] Y. Gao, J. Yin, X. Xu, Y. Cheng, *J. Mater. Chem. A* **2022**, *10*, 9773.
- [10] Z. Liu, L. Li, L. Qin, S. Guo, G. Fang, Z. Luo, S. Liang, *Adv. Mater.* **2022**, *34*, 2204681.

- [11] S. Khamsanga, H. Uyama, W. Nuanwat, P. Pattananuwat, *Sci. Rep.* **2022**, *12*, 8689.
- [12] S. Lee, J. Hwang, W.-J. Song, S. Park, *Batteries & Supercaps* **2022**, *5*, e202200237.
- [13] J. Hu, Y. Qu, F. Shi, J. Wang, X. He, S. Liao, L. Duan, *Adv. Funct. Mater.* **2022**, *n/a*, 2209463.
- [14] L. Dai, Y. Wang, L. Sun, Y. Ding, Y. Yao, L. Yao, N. E. Drewett, W. Zhang, J. Tang, W. Zheng, *Adv. Sci.* **2021**, *8*, 2004995.
- [15] S. Liu, W. Shang, Y. Yang, D. Kang, C. Li, B. Sun, L. Kang, S. Yun, F. Jiang, *Batteries & Supercaps* **2022**, *5*, e202100221.
- [16] H. Yang, W. Zhou, D. Chen, J. Liu, Z. Yuan, M. Lu, L. Shen, V. Shulga, W. Han, D. Chao, *Energy Environ. Sci.* **2022**, *15*, 1106–1118.
- [17] Y. Liu, C. Xie, X. Li, *Angew. Chem. Int. Ed.* **2022**, *n/a*, DOI <https://doi.org/10.1002/anie.202213751>.
- [18] M. Chuai, J. Yang, R. Tan, Z. Liu, Y. Yuan, Y. Xu, J. Sun, M. Wang, X. Zheng, N. Chen, W. Chen, *Adv. Mater.* **2022**, *34*, 2203249.
- [19] H. Chen, C. Dai, F. Xiao, Q. Yang, S. Cai, M. Xu, H. J. Fan, S.-J. Bao, *Adv. Mater.* **2022**, *34*, 2109092.
- [20] J. Heo, S. Chong, S. Kim, R. Kim, K. Shin, J. Kim, H.-T. Kim, *Batteries & Supercaps* **2021**, *4*, 1881–1888.
- [21] X. Shen, X. Wang, Y. Zhou, Y. Shi, L. Zhao, H. Jin, J. Di, Q. Li, *Adv. Funct. Mater.* **2021**, *31*, 2101579.
- [22] D. Wu, L. M. Housel, S. J. Kim, N. Sadique, C. D. Quilty, L. Wu, R. Tappero, S. L. Nicholas, S. Ehrlich, Y. Zhu, A. C. Marschilok, E. S. Takeuchi, D. C. Bock, K. J. Takeuchi, *Energy Environ. Sci.* **2020**, *13*, 4322–4333.
- [23] I. A. Rodriguez-Pérez, H. J. Chang, M. Fayette, B. M. Sivakumar, D. Choi, X. Li, D. Reed, *J. Mater. Chem. A* **2021**, *9*, 20766–20775.
- [24] Z. Liu, Y. Yang, S. Liang, B. Lu, J. Zhou, *Small Structures* **2021**, *2*, 2100119.
- [25] X. Jia, C. Liu, Z. G. Neale, J. Yang, G. Cao, *Chem. Rev.* **2020**, *120*, 7795–7866.
- [26] X. Xie, G. Fang, W. Xu, J. Li, M. Long, S. Liang, G. Cao, A. Pan, *Small* **2021**, *17*, 2101944.
- [27] M. Wang, X. Zheng, X. Zhang, D. Chao, S.-Z. Qiao, H. N. Alshareef, Y. Cui, W. Chen, *Adv. Energy Mater.* **2021**, *11*, 2002904.
- [28] J. Wang, J.-G. Wang, H. Liu, Z. You, Z. Li, F. Kang, B. Wei, *Adv. Funct. Mater.* **2021**, *31*, 2007397.
- [29] J. Li, N. Luo, L. Kang, F. Zhao, Y. Jiao, T. J. Macdonald, M. Wang, I. P. Parkin, P. R. Shearing, D. J. L. Brett, G. Chai, G. He, *Adv. Energy Mater.* **2022**, *n/a*, 2201840.
- [30] J. Ji, H. Wan, B. Zhang, C. Wang, Y. Gan, Q. Tan, N. Wang, J. Yao, Z. Zheng, P. Liang, J. Zhang, H. Wang, L. Tao, Y. Wang, D. Chao, H. Wang, *Adv. Energy Mater.* **2021**, *11*, 2003203.
- [31] S. Wang, Z. Sang, X. Zhao, J. Guo, H. Chen, D. Yang, *Batteries & Supercaps* **2022**, *5*, e202100313.
- [32] G. Wang, Y. Wang, B. Guan, J. Liu, Y. Zhang, X. Shi, C. Tang, G. Li, Y. Li, X. Wang, L. Li, *Small* **2021**, *17*, 2104557.
- [33] G. Cui, Y. Zeng, J. Wu, Y. Guo, X. Gu, X. W. (David) Lou, *Adv. Sci.* **2022**, *9*, 2106067.
- [34] T. Ling, P. Da, X. Zheng, B. Ge, Z. Hu, M. Wu, X.-W. Du, W.-B. Hu, M. Jaroniec, S.-Z. Qiao, *Sci. Adv.* **2022**, *4*, eaau6261.
- [35] J. Chen, W. Xu, H. Wang, X. Ren, F. Zhan, Q. He, H. Wang, L. Chen, *J. Mater. Chem. A* **2022**, *10*, 21197–21250.
- [36] Y. Zhao, R. Zhou, Z. Song, X. Zhang, T. Zhang, A. Zhou, F. Wu, R. Chen, L. Li, *Angew. Chem. Int. Ed.* **2022**, *n/a*, DOI <https://doi.org/10.1002/anie.202212231>.
- [37] Y. Wu, Z. Zhu, Y. Li, D. Shen, L. Chen, T. Kang, X. Lin, Z. Tong, H. Wang, C. Lee, *Small* **2021**, *17*, 2008182.
- [38] W. Gong, B. Fugetsu, W. Mao, A. K. Vipin, I. Sakata, L. Su, X. Zhang, M. Endo, *J. Mater. Chem. A* **2022**, *10*, 15415–15426.
- [39] T. Xiong, Z. G. Yu, H. Wu, Y. Du, Q. Xie, J. Chen, Y.-W. Zhang, S. J. Pennycook, W. S. V. Lee, J. Xue, *Adv. Energy Mater.* **2019**, *9*, 1803815.
- [40] B. Yang, X. Cao, S. Wang, N. Wang, C. Sun, *Electrochim. Acta* **2021**, *385*, 138447.
- [41] Y. Fu, Q. Wei, G. Zhang, X. Wang, J. Zhang, Y. Hu, D. Wang, L. Zuin, T. Zhou, Y. Wu, S. Sun, *Adv. Energy Mater.* **2018**, *8*, 1801445.
- [42] B. Yang, D. Li, S. Wang, C. Sun, N. Wang, *ACS Appl. Mater. Interfaces* **2022**, *14*, 18476–18485.
- [43] J. Wang, J.-G. Wang, H. Liu, Z. You, C. Wei, F. Kang, *J. Power Sources* **2019**, *438*, 226951.
- [44] P. Ruan, X. Xu, D. Zheng, X. Chen, X. Yin, S. Liang, X. Wu, W. Shi, X. Cao, J. Zhou, *ChemSusChem* **2022**, *15*, e202201118.
- [45] Y. Zeng, Y. Wang, Q. Jin, Z. Pei, D. Luan, X. Zhang, X. W. (David) Lou, *Angew. Chem. Int. Ed.* **2021**, *60*, 25793–25798.
- [46] D. Guo, W. Zhao, F. Pan, G. Liu, *Batteries & Supercaps* **2022**, *5*, e202100380.
- [47] Y. Liu, Z. Qin, X. Yang, X. Sun, *Adv. Funct. Mater.* **2022**, *32*, 2106994.
- [48] X. Chen, P. Ruan, X. Wu, S. Liang, J. Zhou, *Acta Phys. Chim. Sin.* **2022**, *38* (11), 2111003.
- [49] G. Ou, Y. Xu, B. Wen, R. Lin, B. Ge, Y. Tang, Y. Liang, C. Yang, K. Huang, D. Zu, R. Yu, W. Chen, J. Li, H. Wu, L.-M. Liu, Y. Li, *Nat. Commun.* **2018**, *9*, 1302.

Manuscript received: November 1, 2022

Revised manuscript received: December 13, 2022

Accepted manuscript online: December 18, 2022

Version of record online: January 5, 2023